

Proximate damped Lyman- α systems as tracers of quasar feedback

Patrick Petitjean

Institut d'Astrophysique de Paris and Sorbonne Université, 98bis Boulevard Arago, 75014, France
e-mail: petitjean@iap.fr

Received XX, 20XX

ABSTRACT

Active galactic nuclei (AGN) profoundly affect the interstellar medium of their host galaxies through intense radiation fields and powerful winds. Characterising this feedback is essential for understanding galaxy formation and evolution. Here we revisit the origin of proximate damped Lyman- α absorbers (PDLAs), which trace cold gas within 3000 km s^{-1} of the quasar redshift, and interpret their kinematics and physical properties within a unified framework. We searched the SDSS DR16 database for low-ionisation metal absorption-line systems at the quasar redshift (referred to as ProxSys). This approach enables us to identify and classify different types of proximate absorbers, including so-called Ghostly systems, coronagraphic DLAs (DLA-Cor), standard DLAs, and sub-DLAs, based on the presence of strong Lyman- α absorption, partial covering signatures, or excited atomic transitions such as Si π^* . We find that about 13% of ProxSys belong to the Ghostly or DLA-Cor classes and exhibit strong absorption from excited species. The different classes of ProxSys form a continuous sequence characterised by decreasing Si π^* , C IV, and N V absorption strengths and dust content. Their velocity distributions reveal multiple kinematic components. Standard DLAs cluster within $\pm 1000 \text{ km s}^{-1}$ of the quasar systemic redshift, consistent with gas in the host galaxy, whereas Ghostly and Si π^* -bearing systems display broader distributions, including outflows reaching -2000 km s^{-1} and a smaller population of inflowing clouds up to $+1200 \text{ km s}^{-1}$. Median stacked spectra confirm that Ghostly and coronagraphic systems arise in dense, compact gas partially covering the quasar emission regions. These results support a scenario in which cold, dense clouds participate in a dynamic cycle of inflow and outflow in the vicinity of quasars, consistent with chaotic cold accretion.

Key words. Galaxies: ISM – Galaxies: Formation – Quasar: Absorption Lines

1. Introduction

Bright quasars at high-redshift are luminous sources powered by the accretion of material from their host galaxies onto a massive black hole. Their intense emission, together with the launching of powerful winds, affects the interstellar medium of the galaxy, either inhibiting or promoting star formation (e.g. Dubois et al. 2013). This feedback is thought to play a major role in galaxy evolution by quenching or enhancing star-formation (e.g. Springel et al. 2005; Cattaneo et al. 2009; Schaye et al. 2015; Dubois et al. 2016; Piotrowska et al. 2022; Bluck et al. 2023; Laužikas & Zubovas 2024).

Active galactic nuclei (AGN) show evidence for multi-phase, multi-scale winds covering a wide range of ionisation states and spatial scales (Laha et al. 2021). In X-rays, a variety of absorption features trace highly ionised, fast outflows. Soft X-ray “warm absorbers” are common, detected in roughly $\sim 50\%$ of radio-quiet AGN (Laha et al. 2014), and typically exhibit velocities of a few hundred up to a few thousand km s^{-1} . More dramatically, ultra-fast outflows (UFOs) are revealed through blue-shifted Fe K-shell absorption lines, indicating highly ionised gas accelerated to relativistic velocities of $\sim 0.1\text{--}0.3 c$. As many as $\sim 40\%$ of nearby AGN show evidence for UFOs originating on sub-parsec scales (Tombesi et al. 2011; Gofford et al. 2015), suggesting that powerful, highly ionised winds are a relatively common feature of accreting supermassive black holes.

In the UV and optical, 15 to 20% of AGNs exhibit blue-shifted high ionisation absorption lines (C IV, N V, O VI...) often in the form of Broad Absorption Line (BAL) systems

(Weymann et al. 1981; Gibson et al. 2009), with outflow velocities up to a few $10^3\text{--}4 \text{ km s}^{-1}$. The variations of the absorptions (Filiz Ak et al. 2012; Aromal et al. 2024) argue for the gas being located close to the accretion disc although ionisation arguments yield to much larger distances (Arav et al. 2020).

BAL winds are radiatively driven, and the enhanced UV reddening of BAL quasars relative to non-BAL quasars indicates that both line absorption and dust radiation pressure contribute to accelerating the outflow (Laor & Brandt 2002). Murray & Chiang (1995) explain that the inner edge of the disc wind giving rise to BALs has the same characteristics as a “warm absorber”. Tombesi et al. (2013) conclude that X-ray UFOs and the comparatively lower velocity warm absorbers could represent parts of a single large-scale stratified outflow observed at different locations from the black hole. Actually, although a distinction between the outflows is made because they are detected with different techniques, they may share similar origin although not located at the same distance to the central AGN (e.g. Bu & Yang 2021).

AGN ionised winds are observed on much larger scales (Zakamska et al. 2016; Leung et al. 2019; Förster Schreiber et al. 2019). Outflows are detected in 17% of the AGNs in the redshift range $1.4 \leq z \leq 3.8$ with spatial extents of 0.3-11 kpc and velocities in the range $400 - 3000 \text{ km s}^{-1}$. Temple et al. (2024) have found a weak correlation between the velocities of the [O III] emission and associated C IV BALs. They conclude that this is consistent with a scenario wherein BAL troughs are intermittent tracers of persistent quasar outflows.

Neutral and molecular outflows are commonly seen from nearby AGNs (Rupke et al. 2021) to high-redshifts (Davies et al. 2024). They are thought to be the consequence of the action of AGN winds onto the ISM of the host-galaxy. They can be traced from the inner region of the AGN in the radio (Morganti et al. 2020) to large scales (Belli et al. 2024). However how these large scale outflows that may quench star formation in the galaxy are launched and how radiation and particle outflows couple with the host galaxy gas is still a matter of debate.

Disc wind outflows are the most efficient way to deposit energy in and out of the AGN host-galaxy. Current theoretical understanding of active galactic nucleus outflows tells that a constant velocity momentum-driven wind is rapidly accelerated following inefficient Compton cooling of post-shock material (Marconcini et al. 2025). Indeed, it seems probable that outflows are energy conserving. Although this has been demonstrated for fast launching winds ($v \sim 10,000 \text{ km s}^{-1}$), slower winds ($v \sim 1000 \text{ km s}^{-1}$) are also possible (Faucher-Giguère & Quataert 2012).

Winds and radiation from the central AGN compress and stir the neutral gas in and around the host galaxy. It is therefore expected that some signature of this interaction should be imprinted in the quasar spectrum as H I absorption, in particular as proximate damped Lyman-alpha systems (DLAs) with small velocities relative to the quasar (typically $\Delta V < 3000 \text{ km s}^{-1}$).

Ellison et al. (2002) searched for DLAs in a radio-selected QSO sample and found that the density of proximate DLAs (PDLAs) is about four times higher than that of intervening systems. No excess of proximate DLAs was found in a radio-quiet sample, however. This result was partially confirmed by Prochaska et al. (2008), who reported that the density of proximate DLAs is roughly twice that of intervening DLAs in the redshift range $2.5 < z < 3.5$, and otherwise consistent. However considering that the observed enhancement of PDLAs around quasars is the result of quasar-galaxy clustering they estimate that the number of proximate DLAs is smaller by a factor of 5 to 10 than expected, interpreting this as the result of the quasar ionising flux photo-evaporating H I in the host and nearby galaxies.

Later, Ellison et al. (2010, 2011) studied, respectively, seven proximate DLAs observed at high resolution and 85 systems from SDSS DR5. They found that proximate DLAs generally have higher metallicities than intervening absorbers, and interestingly, that absorbers near QSOs with lower rest-frame UV luminosities exhibit significantly stronger metal lines. They speculate that absorbers near high-luminosity QSOs may have experienced premature quenching of star formation. H I has also been observed in absorption in the halos of bright quasars within 100 kpc (Prochaska & Hennawi 2009).

It is however known that the clouds giving rise to proximate DLAs can be sufficiently small that they do not fully cover the narrow-line region (so-called coronagraph DLAs or DLA-Cor, Hennawi et al. 2009; Finley et al. 2013; Jiang et al. 2016; Pan et al. 2018; Xie et al. 2018; Balashev et al. 2020), or even the broad-line region (so-called Ghostly DLA, Fathivavari et al. 2017). These systems have been observed across a wide range of quasar types (Wampler et al. 1995; Dai et al. 2020; Gupta et al. 2022; Wu et al. 2024; Rojas-Ruiz et al. 2025). The corresponding clouds have been claimed to be located close to the AGN (Laloux & Petitjean 2021). Recently Noterdaeme et al. (2019) observed an excess of H₂ bearing PDLAs. They conclude that although most of the systems probably originate from galaxies in the quasar group, a small fraction of them could be located in the quasar host itself.

Here, we revisit the nature of proximate DLAs in light of recent observations and simulations, substantially increasing the available statistics thanks to the SDSS DR16 dataset. In Section 2, we describe our procedure to detect proximate systems and classify them into different categories. Section 3 presents the number of systems, while Section 4 shows the median spectra of the various classes. In Section 5, we examine their velocity distributions, and Section 6 discusses the properties of the quasars. We interpret our findings in Section 7 and summarise our conclusions in Section 8.

2. The procedure

2.1. Definitions

We aim to investigate the presence of gas with high H I column density in the vicinity of the active nucleus. Such gas is usually detected through its H I Lyman- α absorption signature in the quasar spectrum at relative velocities less than about 3000 km s^{-1} with respect to the quasar redshift. We refer to these absorption systems as proximate systems (ProxSys) in general. Among these, we call, as usual in the literature, proximate DLAs (PDLA) systems with H I column density $\log N(\text{H I}) > 20.3$. These systems have been searched for in several SDSS releases, and corresponding catalogues are available (Noterdaeme et al. 2012; Chabanier et al. 2022).

However, since our work relies on SDSS data, it is difficult to impose such an arbitrary column density threshold because the low resolution and signal-to-noise ratio of SDSS spectra make damping wings of the Lyman- α trough hard to detect. Also in such spectra only lower limits on the equivalent width can be derived. We therefore do not restrict our sample to DLAs alone, and also include sub-DLAs. In addition, ProxSys include Ghostly and DLA-Cor systems that cannot be detected by their Lyman- α trough.

If we wish to probe the full population of ProxSys down to H I column densities close to, or even somewhat smaller than those of PDLAs, a different selection strategy is required, which does not use the presence of a strong H I Lyman- α trough.

We thus select all absorption systems that can be identified through strong metal lines, without reference to their H I content. Although this is beyond the scope of the present paper, this approach may allow us to distinguish between gas expelled by the AGN, which is expected to be metal-rich, and gas originating from the IGM, presumably of lower metallicity.

2.2. Search for metallic ProxSys

We use the final SDSS-IV quasar catalogue from Data Release 16 (DR16) of the extended Baryon Oscillation Spectroscopic Survey (eBOSS; Dawson et al. 2016; Ahumada et al. 2020), which we will refer to as DR16Q. This catalogue contains 750,414 quasars (Lyke et al. 2020).

We select quasars with quasar redshift, absorption index (characterising the strength of BALs) and median signal-to-noise ratio, $z_{\text{em}} > 2.11$, $\text{AI_CIV} < 1000 \text{ km s}^{-1}$, and $\text{SN_MEDIAN_ALL} > 1.95$. We use the best available redshift as reported on line 27 of Table D1 in Lyke et al. (2020). The minimum redshift threshold is chosen so that we can estimate the strength of the Lyman- α absorption associated with the ProxSys. The C IV absorption index (AI_CIV) is used to avoid broad absorption lines. The minimum SNR is set arbitrarily, based on a few visual inspections, to avoid very noisy spectra and minimise

false positives. After applying these criteria, we are left with a total of 164,901 quasars.

We first applied a simple algorithm to select metal line systems, summing the velocity windows from -3000 to $+3000$ km s^{-1} around the rest wavelengths of the transitions Si π 1260, Si π^* 1264, C π 1334, Al π 1670 at the redshift of the quasar and derive the position of a minimum in the resultant spectrum. We then calculated the equivalent widths and corresponding errors for all transitions above 1200 \AA at the redshift of this position and selected systems with at least two high ionisation transitions (from the N ν and C ν doublets) and two low-ionisation transitions (from the Si π 1260, Si π^* 1264, O π 1302, C π 1334 and Al π 1670 transitions) detected at the 3σ level. These transitions often lie in the wavelength regions of highest SNR. The Mg π doublet is not used at this stage because a number of spectra are spoiled in the corresponding wavelength region by inadequate sky subtraction. We use it during the confirmation process. The required number of detected transitions was chosen to minimise false positives. Note however, that a few H_2 bearing proximate systems without detected high ionisation transitions are known (Noterdaeme et al. 2019). These systems are indeed interesting and could be studied separately, but they are rare. Following this procedure we detected 5373 metal ProxSys candidates.

2.3. Visual inspection

To confirm the reality of the ProxSys, we visually inspected the 5373 spectra selected as described in the previous section. A total of 1071 systems turned out either to be fakes (940) or could not be firmly classified (131), and 45 quasars were identified as BALs missed by DR16. For the remaining 4257 confirmed metal-line ProxSys, we measured the equivalent width of the associated H I absorption when present. Given the spectral resolution and SNR of the spectra, this measurement is highly uncertain, especially since the absorption lies on top of the quasar Lyman- α emission. We therefore arbitrarily classified the systems as HighWSys, LowWSys and VeryLowWSys as those with $W(\text{Lyman}\alpha) > 5$, between 2 and 5, and < 2 \AA , respectively.

We then sorted the systems into several classes: (i) HighWSys or HighWSys?, (ii) LowWSys or LowWSys?, (iii) VeryLowWSys or VeryLowWSys?, where the question mark indicates doubtful cases, mostly due to blending. We also defined more specific classes: (iv) DLA-Cor and DLA-Cor?, corresponding to coronagraphic DLAs when a narrow emission line is present at the bottom of a detected DLA trough; the question mark indicates systems where no emission line is seen but the trough does not reach zero flux, indicating some leakage; (v) Ghost and Ghost?, referring to systems where no or very little absorption is detected at the position of the Lyman- α line, with the question mark indicating ambiguous cases due to low SNR or slightly shifted absorption relative to the metal lines. In addition to these classes, we defined an additional class as ProxSys* gathering all systems from the above classes where absorption from Si π^* 1264 is clearly detected. Other absorption lines are usually too weak to be detected in individual spectra and C π^* 1335 is always badly blended with C π 1334. The selection has been performed with great care, but some low-level contamination by interlopers may still be present.

Particular attention was given to Ghost systems and a second visual inspection was performed. Among the 220 systems classified as Ghost (90) or Ghost? (130), we confirmed 95 Ghost systems and 94 probable Ghosts, and rejected 31. Since these sys-

tems are of particular interest for characterising the spatial distribution of the Broad Line Region (see Laloux & Petitjean 2021), we will report their properties in more details in a forthcoming paper. For the other classes, we find 1688 (resp. 60) HighWSys (resp. HighWSys?), 227 (resp. 96) DLA-Cor (resp. DLA-Cor?), 1554 (resp. 250) LowWSys (resp. LowWSys?), and 119 (resp. 43) VeryLowWSys (resp. VeryLowWSys?).

Note that Ghost and DLA-Cor systems have been shown to be associated with DLAs. Out of a total of 3873 ProxSys, we have identified 189 highly probable Ghosts and 323 DLA-Cor systems. Together, these two categories therefore account for about 13% of the metal-rich ProxSys.

For each detected system, we automatically measured the equivalent width (W) of the Lyman- α absorption line. The distributions of W for HighWSys, LowWSys, VeryLowWSys and DLA-Cor are shown in Fig. 1. We caution that this measurement is only a rough estimate of W , because we measure solely the central portion of the absorption trough, which lies within the wing of the Lyman- α emission line. The resulting values should therefore be considered lower limits on the true effective equivalent width. It is interesting to note that, although the probability of coronagraph DLAs having large equivalent widths is higher compared to the overall ProxSys distribution, they are nevertheless observed across the full range of equivalent widths.

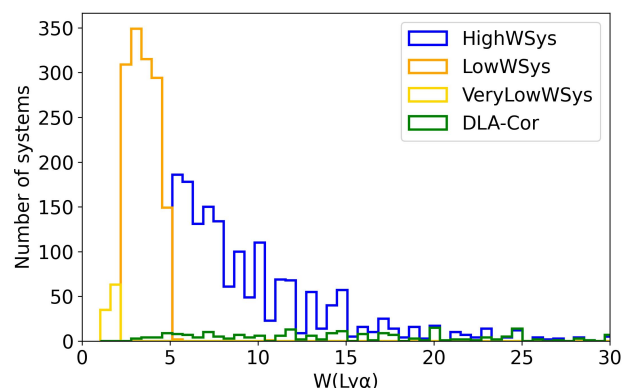


Fig. 1: Distributions of the H I Lyman α absorption line equivalent width for HighWSys (blue), LowWSys (orange), VeryLowWSys (yellow) and DLA-Cor (green) as defined in the text.

We checked whether we recover the Ghostly DLAs detected by Fathivavsari (2020). Out of the 89 systems, we recover 58. Of the 31 missing systems, seven (7) are misidentified Ghostly DLAs, nine (9) are questionable (including three with $1000 > \text{AI} > 900$ km/s), and nine (9) lie outside our search range (four with $\text{AI} > 1000$ km/s and five with $z < 2.11$). Therefore, we miss six confirmed Ghostly DLAs, yielding a success rate of 86%. Among these six, three have no C π line detected but are confirmed by strong Mg π absorption, while three show no high-ionisation absorption lines. This explains why these systems were missed. On the other hand, we find 36 additional confirmed Ghostly DLAs and 94 probable ones. A detailed analysis of these systems will be presented in a future paper.

Out of the 81 systems in Noterdaeme et al. (2019) consisting of systems detected solely via the presence of molecular hydrogen, apart from those outside our selection, we miss nine (9), four of which showing no metals at all. PDLAs without metals or high-ionisation associated lines although rare are of particular interest and may be studied in future work.

We thus conclude that we recover most of the systems already known but more importantly detect twice as much Ghostly DLAs.

3. Number of metal ProxSys

3.1. Comparison with PDLAs

We aim to compare Metal ProxSys systems with PDLAs. To do so, we require a catalogue of PDLAs identified through their Lyman- α absorption trough. PDLAs have been searched for in SDSS-DR5 by Prochaska et al. (2008) (for $\log N(\text{H I}) > 20.3$) and in SDSS-DR9 and SDSS-DR16 by, respectively, Noterdaeme et al. (2012) and Chabanier et al. (2022) (for $\log N(\text{H I}) > 20$).

Chabanier et al. (2022) provide a catalogue of PDLAs which appears at first sight to be suitable for our purpose. However, we realised that their DLA search was performed only up to the quasar emission redshift, z_{em} , whereas PDLAs can be detected with $z_{\text{abs}} > z_{\text{em}}$. Keeping this limitation in mind and because it is derived from the same data release as our work, we nevertheless make use of their catalogue for the present comparison.

In Fig. 2, we plot the velocity of the systems relative to the quasar emission redshift for the PDLAs in DR16 with $\log N(\text{H I}) > 20$, as reported by Chabanier et al. (2022), together with our HighWSys sample. It is apparent that PDLAs with $z_{\text{abs}} > z_{\text{em}}$ are not included in the Chabanier's sample. It is worth noting on Fig. 2 that the shapes of the distributions are similar (see below however). In addition there is a peak at z_{em} and a minimum around -1000 km s^{-1} which stayed unnoticed in previous studies.

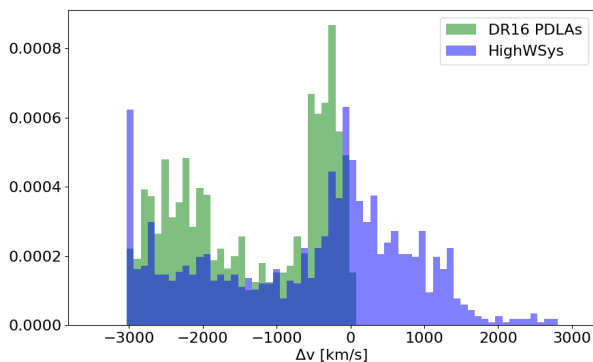


Fig. 2: Distributions of the velocity difference between the system and the quasar for the HighWSys ProxSys (blue) and the PDLAs in Chabanier et al. (2022) (green).

In Fig. 3 we plot the equivalent width of the Lyman- α trough measured for our systems versus the logarithm of the H I column density as measured by Chabanier et al. (2022). The blue, orange and red points correspond to High, Low and Verylow-W systems respectively. There are 710 systems common to our and Chabanier's samples, 524, 184 and 2 High, Low and Verylow-W systems, respectively. It is clear that most of our systems are bona fide DLAs or sub-DLAs and that the corresponding equivalent widths are underestimated. The distributions of $\log N(\text{H I})$ for these systems as measured by Chabanier et al. (2022) are given in Fig. 4.

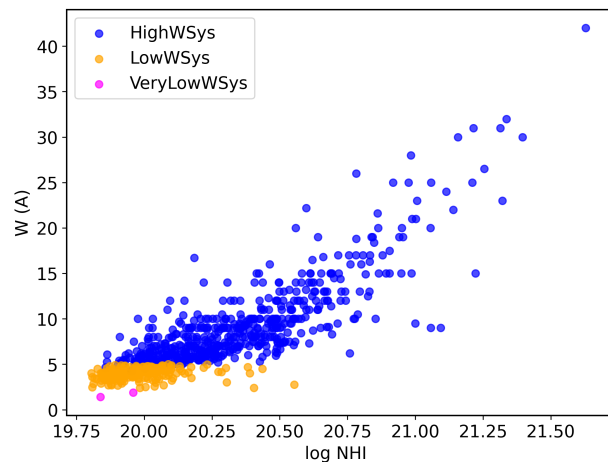


Fig. 3: Equivalent width of the Lyman- α trough measured for our systems versus the logarithm of the H I column density as measured by Chabanier et al. (2022). The blue, orange and red points correspond to High, Low and Verylow-W systems.

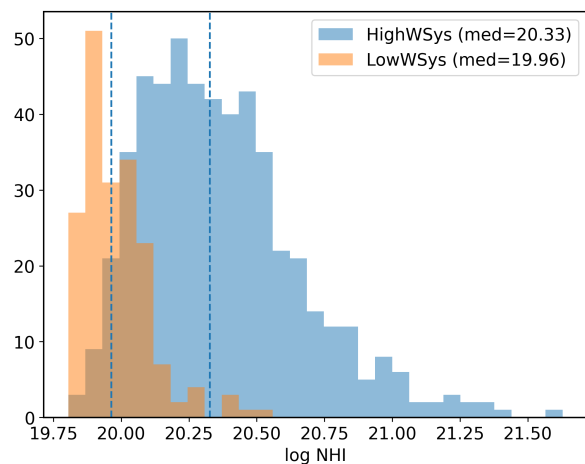


Fig. 4: Distributions of the H I column densities for High- (blue) and Low- (orange) Wsys for the 770 systems common to our and Chabanier's samples.

The fact that we recover 710 systems from the Chabanier's catalogue implies that we recover a significant fraction ($>20\%$) of bona-fide PDLAs.

3.2. Distribution with redshift

In Fig. 5 we plot the distribution of the ratio of HighWSys (blue), Ghost (including probable Ghost) (green) and PDLAs in DR16 (black) from Chabanier et al. (2022) to the number of quasars in DR16 (with the same selection criteria) versus redshift. The ratio is multiplied by a factor of five for Ghost DLAs. It is striking to note that although the number of PDLAs increases with redshift, the number of systems detected in this work does not. The ratio of our systems to the total number of quasars is remarkably constant. The surprising low number of PDLAs detected at $z < 2.4$ may be due to the fact that it is more difficult to detect them at the blue end of the spectrum whereas we do not have this difficulty for metal line systems. This could be a consequence of the presence of much more gas with low metallicity at high redshift but more probably a consequence of a mixture of all this. Note

also that this may explain in part the large number of our systems that are not in the PDLA sample.

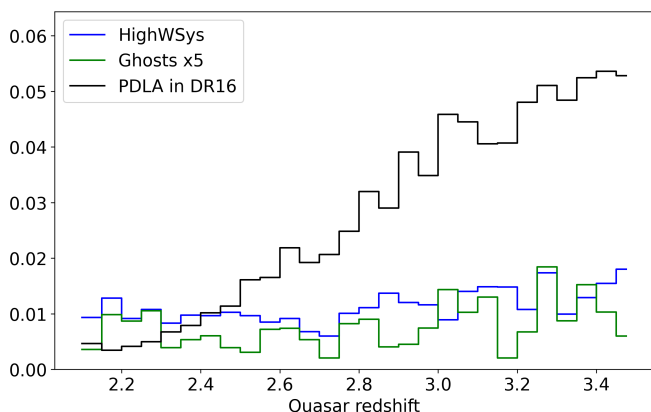


Fig. 5: Ratio of the number of PDLAs in Chabanier et al. (2022) (black), HighWSys (blue) and Ghost+Ghost? (green) to the total number of DR16 quasars with the same selection criteria. The ratio is multiplied by a factor of five for Ghost DLAs.

4. Median spectra

In this section, we derive a median spectrum for several of the system classes defined above, allowing us to distinguish them on a physical basis. To do so, we stack the spectra of the corresponding quasars after shifting them to the rest frame of the absorbers.

For the Ghost and Ghost? systems, we obtained the median spectra separately and found them to be very similar, except that the H I absorption is slightly more pronounced in the Ghost? class. We therefore combined all Ghost and Ghost? systems into a single sample. In Fig. 6, we show the median spectrum of the combined Ghost+Ghost? sample in green together with that of the HighWSys in our sample in blue. Both spectra are normalised within a 100 \AA window around 2900 \AA .

It is apparent that the Ghost spectrum is more attenuated, suggesting a larger dust content in Ghost DLAs. In addition, the absorption lines arising from excited levels of Si II and C II are significantly stronger in Ghost DLAs. Although most absorption lines exhibit similar strengths, the Mg II and C IV profiles are noticeably broader in Ghost DLAs (see Fig. 7). Moreover, the absorptions in the Lyman series are strong clearly indicating that Ghost DLAs are bona fide DLA systems.

During the visual inspection, we flagged all systems in which absorption from excited levels of Si II is detected. In Fig. 6, we overplot the median spectrum of these systems on top of the HighWSys spectrum. The strengths of the Si II* and N V absorptions suggest a sequence among the three spectra, indicating exposure to a more intense UV radiation field.

In Fig. 8, we show the median spectra of the DLA-Cor systems with (blue) and without (orange) detectable Si II*. A narrow emission line is visible in the DLA trough for the systems without (or with only weak) Si II* absorption, whereas the systems with strong Si II* absorption display a trough which is not going to the zero level but has no clear narrow emission line. The DLA-Cor* spectrum is also slightly more attenuated. This strongly suggests that the systems with detectable Si II*, DLA-Cor*, represent a transition between DLA-Cor and Ghost DLAs. The absence of a narrow emission line is likely a consequence of

the larger kinematic spread of the DLA-Cor* systems around the QSO redshift, which washes out the emission line.

The number of systems flagged for the presence of Si II* absorption are 54 HighWSys (out of 1688), 101 LowWSys (out of 1554), 17 VeryLowWSys (out of 119) and 48 DLA-Cor (out of 227). Therefore, the peculiar systems (either not covering the whole emission region, DLA-Cor+DLA-Cor?+Ghost+Ghost? or being associated with excited species or both) represent 583 out of 3774 objects (HighWSys+LowWSys+VeryLowWSys in addition to the particular objects) thus 15%.

In Fig. 9 we plot part of the spectrum of these systems (HighWSys, LowWSys and VeryLowWSys) with Si II* detected. It can be seen that (i) the Si II* absorptions are very similar although the H I absorptions are very different; (ii) the C II*/C II ratio but also the N V absorptions are stronger at lower $N(\text{H I})$. We note that there is a small signature of dust attenuation as for Ghostly DLAs (see Fig. 6). It seems that the sub-DLAs* are closer to the central AGN and that the reduced H I column density is a consequence of ionisation.

Finally we compare in Fig. 10 the spectra of HighWSys (blue), HighWSys with Si II* (orange), DLA-Cor with Si II* (green) and Ghostly DLAs (red). It is apparent that there is a sequence HighWSys/HighWSys*/DLA-Cor*/Ghost with higher excitation and ionisation from DLAs to Ghosts revealed by stronger Si II* absorption and C II*/C II ratio plus stronger C IV, N V and O VI absorptions (see also Balashev et al. 2023).

5. Velocity distributions

We study here the kinematics of different classes of absorbers to determine whether this parameter allows us to distinguish between them. In Fig. 11, we show two histograms smoothed using Kernel Density Estimation, representing the distributions of velocities relative to the quasar emission redshift for the different classes.

In the top panel, the blue and orange curves correspond to HighWSys and LowWSys, respectively, with about 1500 objects in each sample. In both cases, two distinct regions are visible. The peak centred near zero velocity corresponds to systems located close to the quasar redshift, likely associated with the host galaxy. The width of this peak, approximately 1400 km s^{-1} full width at half maximum (FWHM), is larger than the uncertainty in quasar redshift, which we estimate to be between 700 and 1000 km s^{-1} (Pâris et al. 2018). This indicates that the neutral gas associated with the galaxy is highly turbulent. There is a minimum in the distributions around -1200 km s^{-1} , beyond which the distribution rises again. This likely corresponds to a deficit of systems caused by the clearing of neutral gas around the galaxy by the strong UV flux. At velocities smaller than -2000 km s^{-1} , we observe the onset of the intervening DLA population.

In the bottom panel, we plot the same distributions for Ghostly DLAs (green curve), all systems where Si II* absorption is detected (purple curve), and DLA-Cor systems with no Si II* absorption (magenta curve), with approximately 200 objects in each sample. These systems correspond to peculiar absorbers identified above, likely located in the central part of the host galaxy, where some clouds either do not fully cover the background emission source or where silicon is excited by the physical conditions characteristic of these regions. Two distinct regimes are apparent. A peak around the quasar redshift, similar to that seen in the top panel, is present. However, in this case, the peak is broader, with a full width at half maximum of about 2200 km s^{-1} . This is the only peak in the distribution of DLA-Cor systems without excited Si II absorption. In contrast,

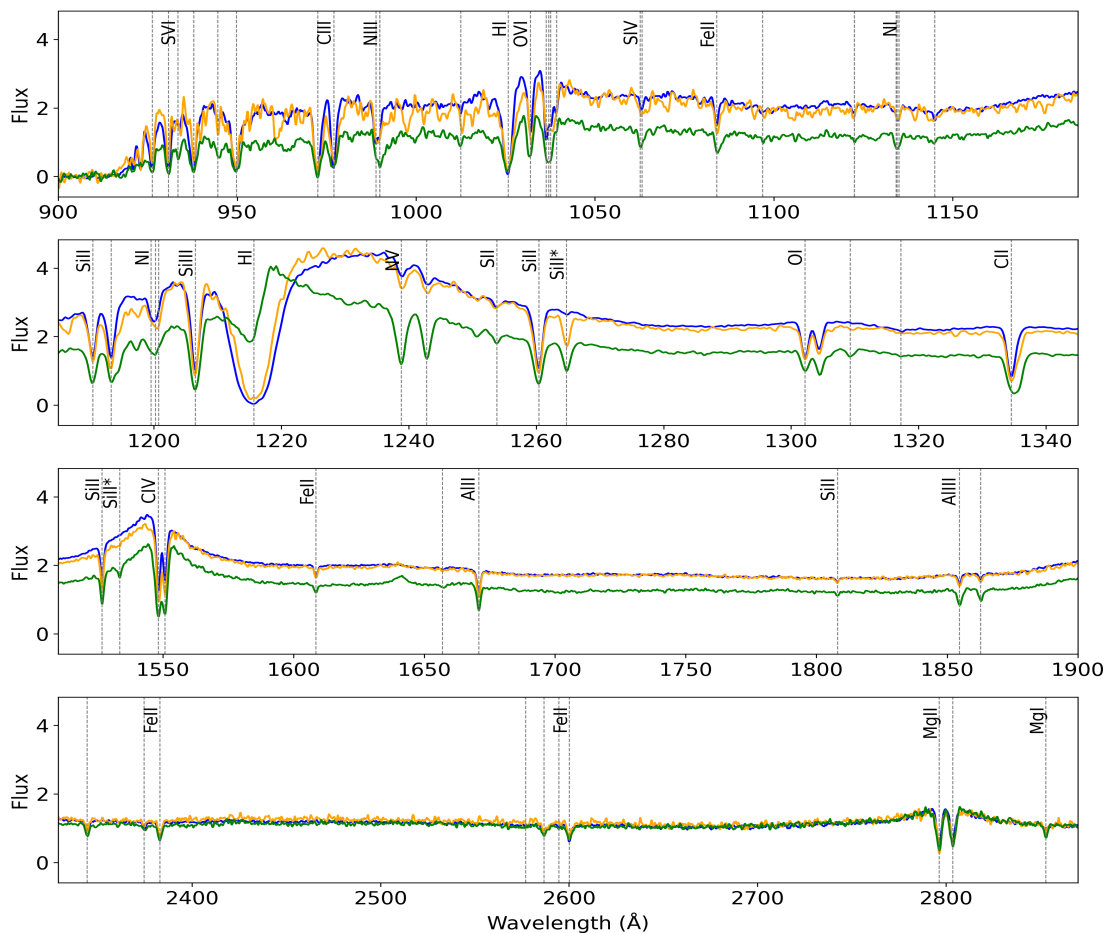


Fig. 6: Median spectra of the Ghost+Ghost? (green), HighWSys (blue) and HighWSys with Si π^* (orange)

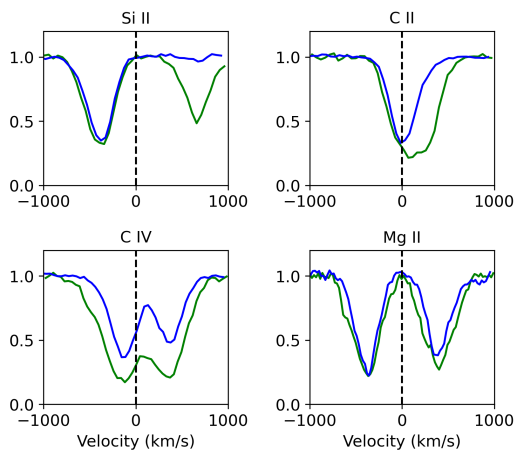


Fig. 7: Portions of the normalised median spectra of HighWSys (blue) and Ghost DLAs (green) around a few transitions. Upper panels: Si π^* λ 1260 and Si π^* λ 1264 on the left, C π λ 1334 and C π λ 1335 on the right. Lower panels: C IV doublet on the left and Mg II doublet on the right.

the other two distributions show a second peak around -1000 to -2000 km s^{-1} . Most Ghost DLAs have such velocities, coinciding with the lack of simple DLAs at these velocities as seen in the top panel. This strongly suggests that these Ghostly DLAs

are part of an AGN-driven outflow. We interpret these observations in Section 7.

6. Quasar properties

Wu & Shen (2022) produced a catalogue of continuum and emission-line properties for broad-line quasars in the SDSS DR16 catalogue (Lyke et al. 2020). Here, we explore the characteristics of the quasars with ProxSys systems using their results.

Fig. 12 shows the g-band versus W2-band magnitudes for quasars in DR16 (black), quasars with PDLAs from the sample of Chabanier et al. (2022) (red), and quasars with Ghost or Ghost? systems from this work (green). It is apparent that quasars with Ghost+Ghost? systems are brighter in W2 while exhibiting similar g-band magnitudes. The median values of g and W2 magnitudes for the three samples are 20.766, 20.944, 20.914 and 16.167, 16.228, 15.613, respectively.

Interestingly, quasars in which a DLA with Si π^* is detected are also brighter in W2, as shown in Fig. 13. The median W2 magnitude for this sample is 15.431.

Fig. 14 shows the bolometric luminosity versus black-hole mass for quasars in DR16 (black), quasars with PDLAs from the sample of Chabanier et al. (2022) (red), and quasars with Ghost+Ghost? systems from this work (green). The median values of M_{BH} and L_{bol} for the three samples are 8.89, 9.05, 8.85 and 46.32, 46.50, 46.30, respectively.

PDLA quasars are slightly more luminous and host marginally more massive black holes. Interestingly, we consis-

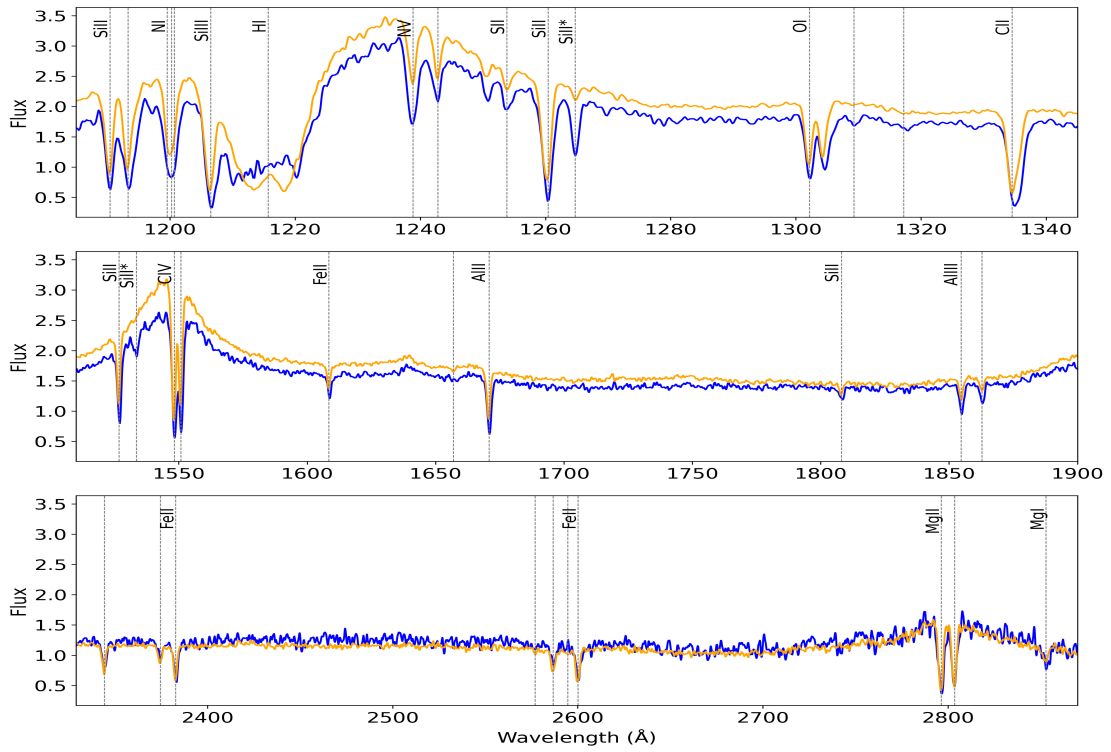


Fig. 8: Median spectra for the DLA-Cor with (blue) and without (orange) Si II^* .

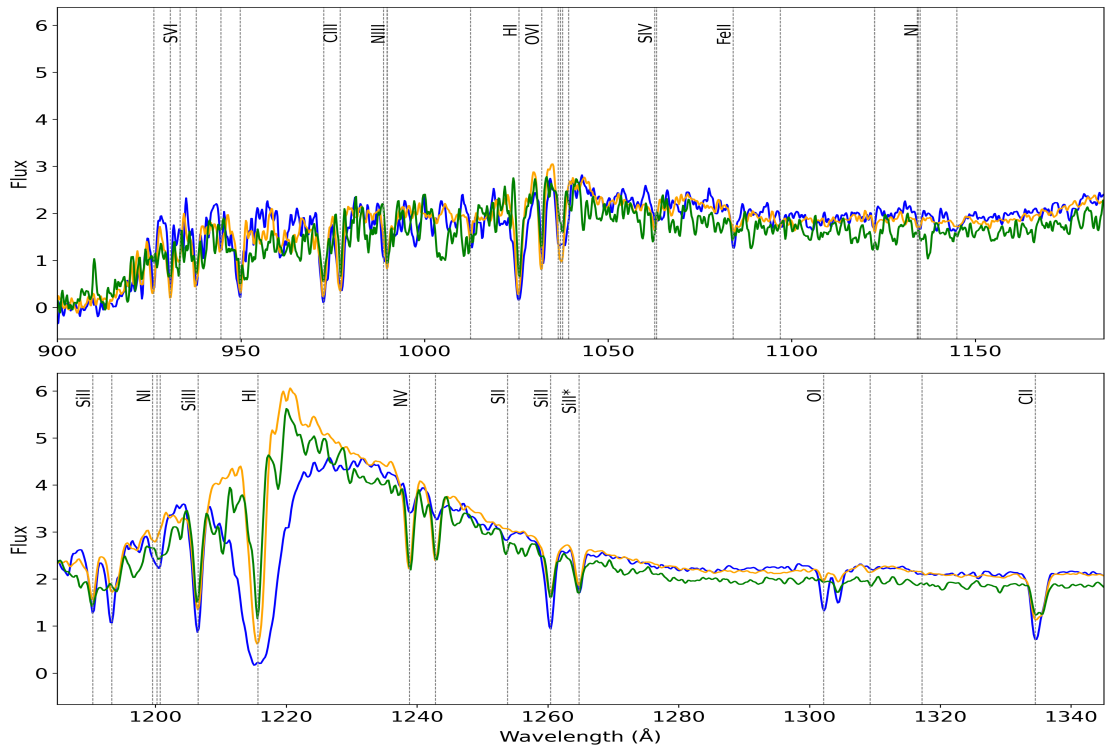


Fig. 9: Median spectra for the HighWSys (blue), LowWSys (orange) and VeryLowWSys (green) with Si II^* absorption detected.

tently recover these differences if we replace the PDLA sample from DR16 with our HighWSys sample. This could reflect the greater prevalence of systems with large velocity offsets relative to the quasar (and thus likely associated with companion galaxies), as seen in Fig. 2, if brighter quasars tend to reside in richer environments (see also Ellison et al. 2010).

Although direct evidence of feedback is difficult to obtain, it has long been suggested that feedback is somehow related to the Eddington ratio (e.g., Fabian et al. 2009). Fig. 15 shows the cumulative distribution of the Eddington ratio for the same three samples. The KS test yields a p-value of 0.018 and 0.0019 between the Ghost distribution and the DR16 quasars and the DR16

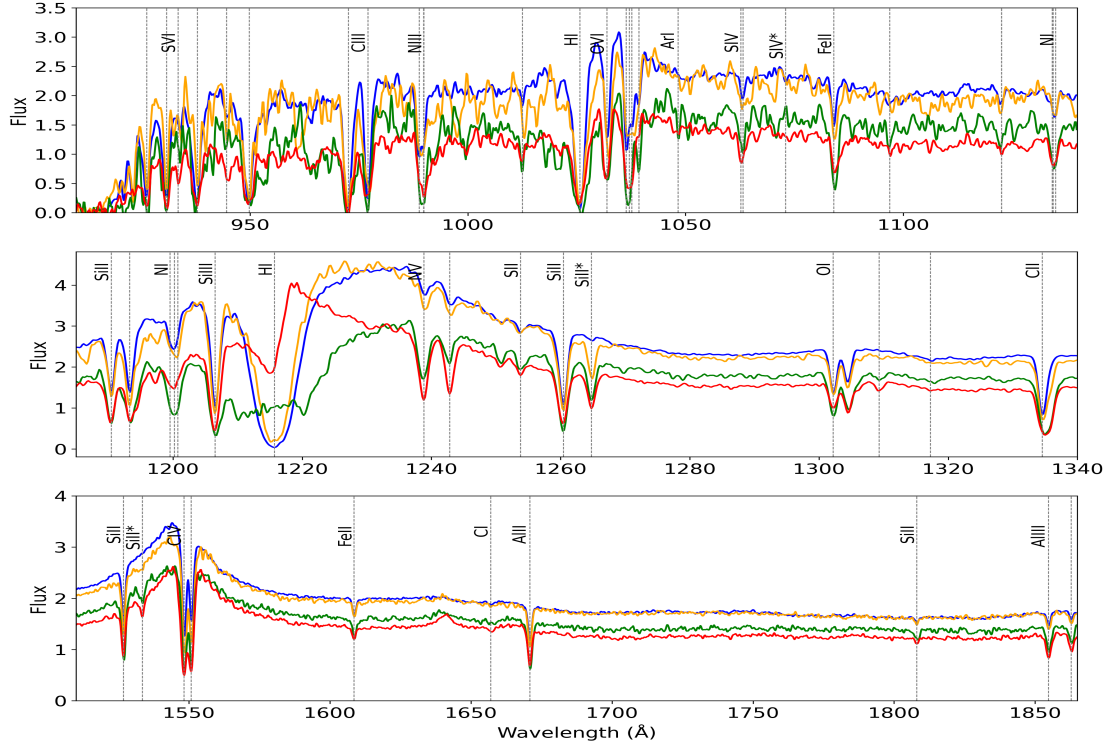


Fig. 10: Median spectra for the HighWSys (blue), HighWSys with Si π^* (orange), DLA-Cor with Si π^* (green) and Ghostly DLAs (red).

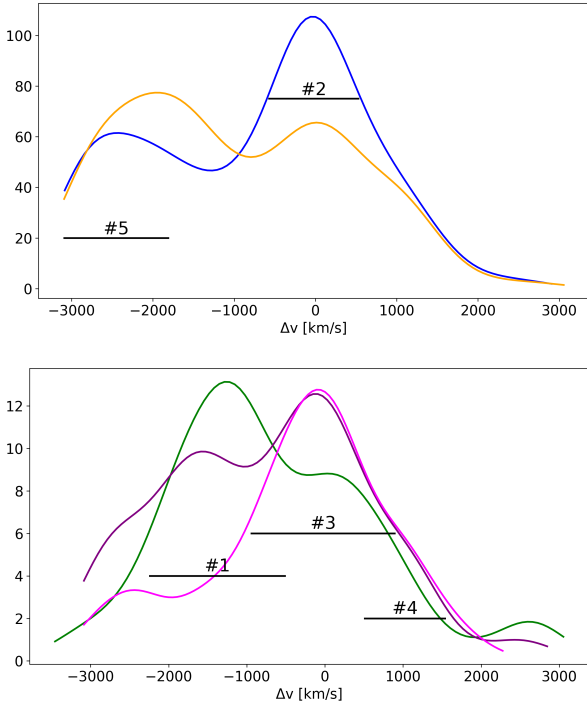


Fig. 11: Distributions of the velocity relative to the quasar for, in the upper panel, HighWSys (blue) and LowWSys (orange), and in the bottom panel, Ghostly DLAs (green), all systems with detected Si π^* absorption (purple) and DLA-Cor without any Si π^* absorption (magenta). The regions #1 to #5 are discussed in Section 7.

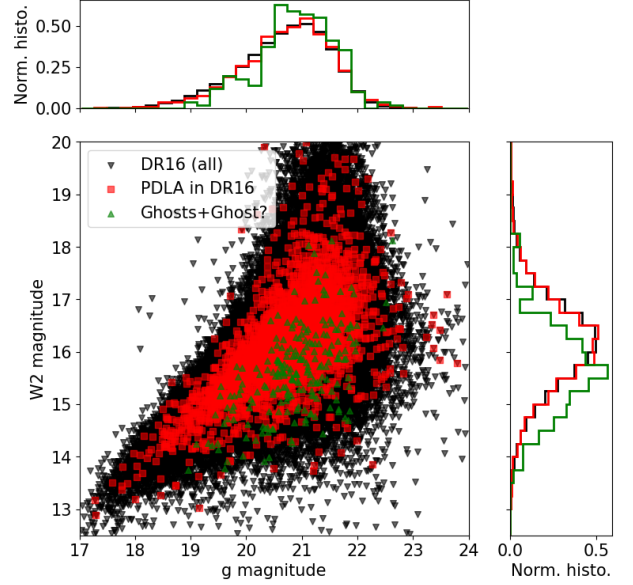


Fig. 12: g magnitude versus W2 magnitude for all DR16 quasars (black), quasars with PDLA from the sample of Chabanier et al. (2022) (red) and quasars with Ghost+Ghost? of this work (green). The histograms of g and W2 are represented on the right and top axis.

PDLAs distributions, respectively, indicating that the distributions are significantly different at the 5% level.

The difference between DR16 quasars and quasars with PDLAs may be explained by the same effect discussed above. More surprisingly, however, is the difference between DR16 quasars and quasars with Ghost+Ghost? systems: there is an excess of

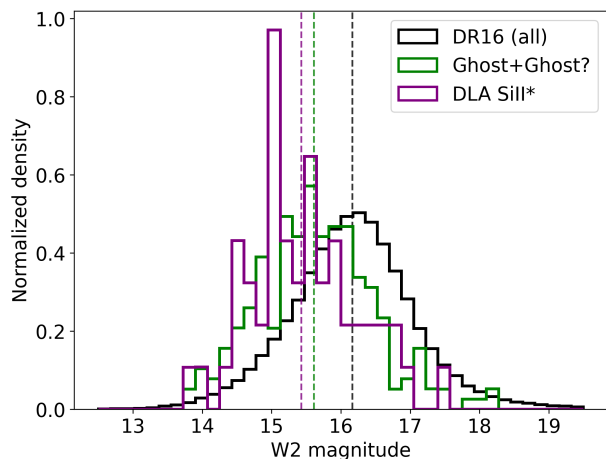


Fig. 13: Normalised histogram of W2 magnitude in the samples of DR16 quasars (black), quasars with Ghost+Ghost? systems (green) and quasars with DLAs showing Si π^* absorption (purple).

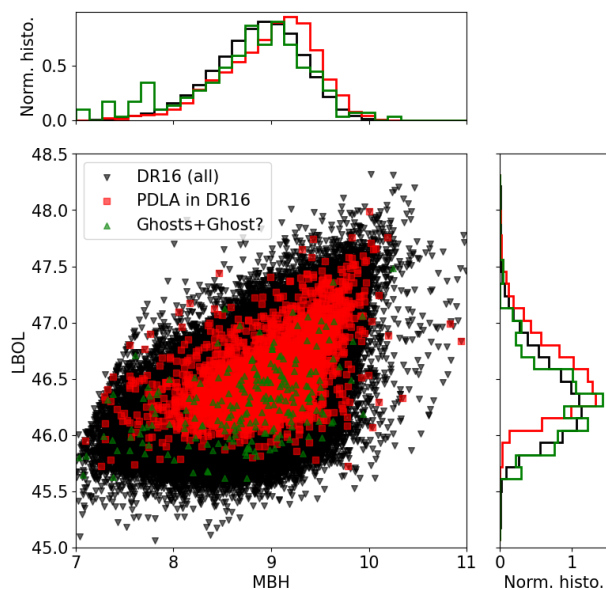


Fig. 14: Bolometric luminosity versus black-hole mass for all DR16 quasars (black), quasars with PDLA from the sample of Chabanier et al. (2022) (red) and quasars with Ghost+Ghost? of this work (green). The normalised histograms of LBOL and MBH are represented on the right and top axis.

the latter at both low and high Eddington ratios as ascertained by an Anderson-Darling test with p-value smaller than 10^{-5} . This will be discussed further in Section 7.

To illustrate this within the Ghost+Ghost? sample, Fig. 16 shows the distributions of black-hole mass (top panel), bolometric luminosity (middle panel), and velocity relative to the quasar (bottom panel) for the two sub-samples with low and high Eddington ratios. Each sub-sample contains 92 systems. Clearly, differences in the Eddington ratio are dominated by black-hole mass, with no significant difference in the velocities between the two sub-samples. Note that the Eddington ratio describes the state of the quasar at the time of observation, whereas the

velocity of the cloud reflects processes occurring on a longer timescale.

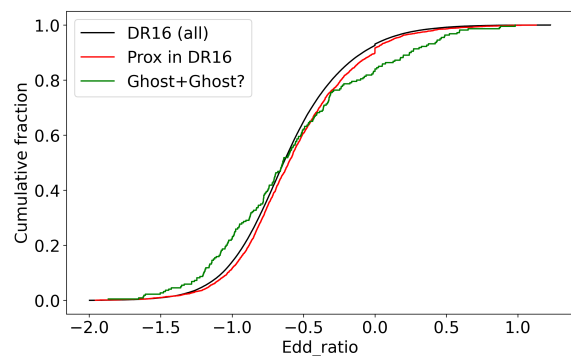


Fig. 15: Cumulative distribution of Eddington ratios for quasars in DR16 (black), DR16 PDLAs (red) and Ghost+Ghost? (green).

We explored the possible correlation between velocity and the characteristics of the quasars. No clear trend was observed, except for a slight dependence on black-hole mass, as illustrated in Fig. 17. Black triangles and contours represent Ghost+Ghost? systems, while red points and contours correspond to HighWSys in our sample. There appears to be a weak tendency for smaller black-hole masses to be associated with smaller velocities in the Ghost sample. There is a statistically significant shift in the location of the KDE maximum ($\Delta MBH = -0.28 \pm 0.07$ and $\Delta V = -989 \pm 286$). Interestingly, Ghost+Ghost? systems are distributed across all black-hole masses, whereas DLAs occur less frequently at lower masses.

7. Discussion

The distributions of the system velocities relative to the quasar redshift (Fig.11), show different components: (i) an outflow component (component #1) with velocities up to $\sim -2200 \text{ km s}^{-1}$ mostly seen in Ghostly systems (small clouds with large density, see below); (ii) two components centred on the quasar redshift: one with smaller dispersion (component #2 seen for HighWSys and LowWSys) originating in gas in the host galaxy, and one with larger dispersion (Ghostly DLAs, systems with Si π^* and DLA-Cor, component #3) a component associated with the host galaxy but with a disturbed kinematics which might correspond to the final fate of the outflow component ; (iii) one component (#4) with positive velocity up to 1800 km s^{-1} which is associated with gas bouncing back to the centre of the quasar and (iv) a component with large negative velocities (#5) corresponding to systems associated with companions of the quasar host galaxy. In the following we will discuss kinematic components #1 to #4. Component #5 corresponds to the standard interpretation of PDLAs and is clearly identified.

7.1. Component #1 and Ghostly systems

A large fraction of the Ghostly systems are apparently part of an outflow with typical velocities in the range -1000 to -2000 km s^{-1} and one can conjecture that the gas in these systems originates from above the disc of the host galaxy, may be the dusty torus, and is driven by radiation or central disc wind.

A detailed study of the physical characteristics of these systems from SDSS data is difficult, if not impossible, as column densities cannot be robustly derived from the absorption features

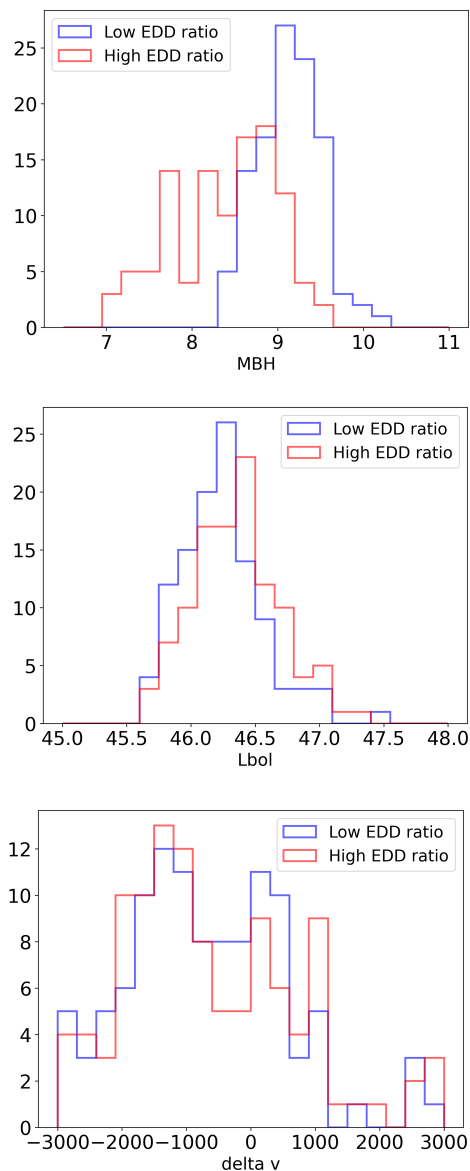


Fig. 16: Top panel: Black-hole mass distributions of quasars with Ghost+Ghost? systems, split into low (red) and high (blue) Eddington-ratio subsamples. Middle panel: Same for the bolometric luminosity. Bottom panel: Same for the velocity of the systems relative to the quasar.

due to the low spectral resolution of the spectra (e.g. Prochaska 2006). The derivation of column densities from such data is a common practice that we will avoid here. We will devote future work to a more detailed characterisation of their properties. We can however discuss some of these characteristics useful here.

The presence of Si π^* can be interpreted by collisional excitation. Other processes, direct pumping by IR radiation or indirect pumping via UV excitation like in the ISM of GRB host galaxies (Vreeswijk et al. 2007) are unlikely, in particular the absence of absorption from the excited level Fe $\pi^6D_{7/2}$ at $\lambda 2396$ favours the collisional excitation origin (Prochaska et al. 2006). From the spectra in Fig.9 we can say that the Si $\pi^*/$ Si π column density ratio is in the range 0.5, if the lines are optically thin, to 1, if they are optically thick. From Silva & Viegas (2002), given that collisions with electrons are the most effective, we can de-

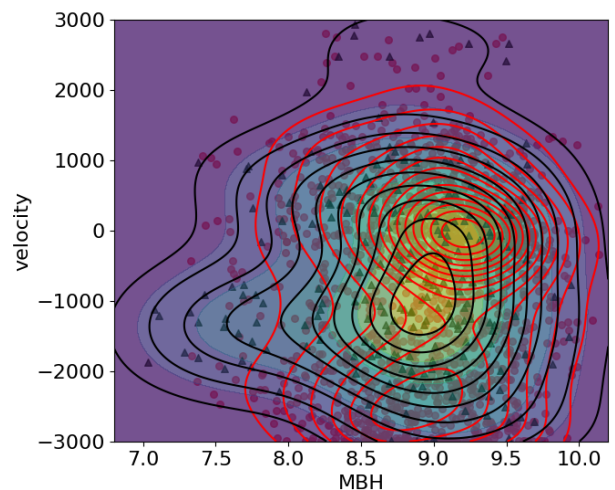


Fig. 17: Velocity of systems versus black-hole mass. Black triangles and contours represent Ghost+Ghost? systems, while red points and contours correspond to HighWSys in our sample

rive (see their Fig. 8) that the electronic density is in the range $200\text{-}1000\text{ cm}^{-3}$ (see also Fig. 6 of Srianand & Petitjean 2000). Same range can be derived from the fact that the C $\pi^*\lambda 1335$ is stronger than the C $\pi\lambda 1334$ line (see Fig. 10).

We can estimate a lower limit on the distance of the Ghost gas from the central engine using the presence of Mg π absorption and following Prochaska et al. (2006). Considering the gas in ionisation equilibrium, a Mg π recombination coefficient of $\alpha = 10^{-12}\text{ cm}^3/\text{s}$, a Mg π ionisation cross-section of $\sigma = 2 \times 10^{-18}\text{ cm}^2$, for a ratio Mg π /Mg $\pi^* = 0.01$, an electronic density of $n_e = 500\text{ cm}^{-3}$ and a flux at 7.6 eV of $F = 10^{-17}\text{ erg/s/cm}^2/\text{\AA}$ we can estimate that the distance to the quasar is larger than 1 kpc. This is large and means probably that the structure of the cloud is more complex. High spectral resolution observation are required to have a better understanding of the physical properties of these clouds. Another but still very uncertain lower limit on the distance can be obtained by equating the heating rate to the cooling rate in the cloud using the constraint on the C $\pi^*/$ C π ratio following Wolfe et al. (2003). Using this constraint, Fathivavsari et al. (2017) found a lower limit of 39 pc. The clouds are not located in the close vicinity of the central engine but are still in its proximity.

If the H I column density is of order 10^{21} cm^{-2} (Fathivavsari et al. 2017), then a characteristic size of the Ghostly clouds would be smaller than 1 pc, explaining the partial coverage of the BLR. Note that partial coverage does not prevent the gas from being far from the centre. Indeed partial coverage is observed frequently for associated systems and BALs (Crenshaw et al. 2003) and corresponding distances of the gas to the centre are sometimes claimed larger than 1 kpc (Borguet et al. 2013; Arav et al. 2018).

Therefore, Component #1 is most likely associated with an outflowing gas located at distances of the order of tens to hundreds of parsecs from the central engine. This interpretation is supported by its kinematics, the large Si $\pi^*/$ Si π and C $\pi^*/$ C π ratios, and the presence of strong associated N ν and O νI absorption, indicating a multiphase medium.

7.2. Component #2

This component corresponds to the standard PDLAs. These are DLAs with velocities relative to the quasar within -1000 to 1000 km s^{-1} . The properties of such systems have been studied by Prochaska et al. (2008) and Ellison et al. (2010). Large distances, up to several tens of kpc, between the corresponding gas and the central engine are found using the Wolfe et al. (2003) method (see also Rix et al. 2007). However, recent studies of similar PDLAs bearing molecular hydrogen place the systems much closer to the central engine.

Noterdaeme et al. (2019) searched for proximate H_2 -bearing DLAs in SDSS DR14 and confirmed 81 systems with velocity offsets relative to the quasar smaller than 3000 km s^{-1} . This represents an excess by a factor of 4–5 compared to the incidence of similar intervening systems. A significant, although generally small, residual flux is observed in the core of the DLA Lyman- α trough for about half of the systems. Absorption from excited atomic levels is detected in at least ten of them. Noterdaeme et al. (2023) investigated the physical and kinematic properties of eleven of these systems and found that their velocity offsets relative to the quasar are within 500 km s^{-1} . These absorbers therefore belong to component #2 or #3. They concluded that the gas is located in the immediate vicinity of the central engine and may be associated with inflowing and/or outflowing material. A similar conclusion was reached by Han et al. (2026) for a PDLA at $z = 2.40$ towards Q2310–3358, for which they derived a particle density of $n_{\text{H}} \sim 1000 \text{ cm}^{-3}$ similar to the density derived for Ghostly systems.

7.3. Component #3

The systems in this component has velocities in the range -1000 to 1000 km s^{-1} but peaked at zero velocity. They are either Ghostly DLAs or systems with Si II^* or DLA-Cor. Their kinematic distribution is broader than the one of the standard PDLAs (#2). They show significant residual in the core of the DLA trough and absorption from excited atomic levels. This indicates that density is high and their typical size is consistently small. They are associated with stronger N V absorptions (see Fig. 10). It is tempting to see this gas as a consequence of the interaction between the outflow and the ISM of the host-galaxy.

7.4. Component #4

It can be seen in Fig. 11 that the velocity distribution of Ghostly systems extends beyond $+1000 \text{ km s}^{-1}$. These systems having the same characteristics as the other Ghostly systems must be of high density and located within a few hundreds pc from the centre. They are however inflowing. There is no clear difference in the spectra of these systems compared to the spectra of other Ghostly systems. This component is seen also for the other types of systems.

Gaspari & Sądowski (2017) developed the so-called chaotic cold accretion (CCA) model, in which gas inflow occurs as cold clouds condense out of the hot medium and migrate towards the centre through inelastic collisions. These cold clumps share similar physical characteristics with those inferred for component #4. The accretion energy is subsequently converted into ultra-fast outflows that entrain warm gas outward. In this framework, the velocities of the warm gas (typically associated with component #1) can reach up to $\sim 1000 \text{ km s}^{-1}$. These clouds are expected to lie at distances of a few hundred parsecs from the nucleus and to exhibit large internal velocity dispersions, as ob-

served in Ghostly systems (Fathivavsari et al. 2017). A region characterised by highly turbulent kinematics may then develop at slightly larger distances, possibly corresponding to component #3.

7.5. Geometry

We can interpret the fact that the Ghostly systems are seen in quasars with brighter W2 magnitude as a geometrical effect if these clouds are located close to the disc of the host galaxy. Indeed, in that case the lines of sight intercepting these clouds have a preferential view of the inner side of the torus where the hot dust is located.

We have found 189 systems (so-called Ghost+Ghost?) where the Lyman- α trough is not or barely seen indicating that the corresponding clouds have transverse sizes smaller than the BLR. We found as well ~ 400 systems showing a noticeable presence of Si II^* . In total this is about 15% of the 4000 systems we flagged in our study or 0.25% of the 164,900 selected quasars in DR16. If the covering factor inside the regions where these clouds reside is of the order of 2% (Gaspari et al. 2018) and if we assume the clouds are located close to the galactic disc, the equatorial angle of the region is 8.5 degrees for Ghostly DLAs and 17 degrees for the systems with Si II^* detected.

7.6. The excess of Ghostly systems at low and high accretion rate

We have seen on Fig. 15 that the distribution of the accretion rate of Ghostly systems show an excess at low and high accretion rates compared to the population of quasars. We could easily imagine that a high accretion rate increases the ambient UV flux. To maintain a large column density of neutral hydrogen, the density of cold condensations would need to increase. In addition, the level of turbulence in the gas would also increase, as would the probability for a given line of sight to intersect such condensations. For low Eddington ratio this seems at first glance more difficult to understand. However, the low Eddington ratio is related to higher BH masses (see Fig. 16). Higher BH masses correspond to deeper potential wells and therefore more turbulence in the CCA scenario. The probability of a given line of sight intersecting a Ghostly system is therefore larger at both extremes.

We should note that Vivek & Wylezalek (2025) show that the BAL fraction is increasing both at high and low Eddington ratios.

8. Conclusion

PDLAs have long been considered to be associated with gas in companion galaxies of the quasar host galaxy. The underlying idea is that gas in the host galaxy itself should be preferentially ionised by the central ionising source (Prochaska et al. 2008; Ellison et al. 2010). Indeed, Hennawi & Prochaska (2007) showed that the probability of detecting an absorber with a high neutral hydrogen column density is much lower along the line of sight to the quasar than in the transverse direction (see also Guimarães et al. 2007; Perrotta et al. 2016). They conclude that this is a consequence of absorbers along the line of sight being photo-evaporated by direct exposure to the quasar's ionising radiation. However, their Fig. 6 shows that a cloud can survive within ~ 10 kpc of the quasar provided its density exceeds $\sim 10^3 \text{ cm}^{-3}$, which is consistent with the density we infer from the presence of Si II^* absorption in at least part of these systems.

More recently, the detection of H₂-bearing clouds at the quasar redshift (Noterdaeme et al. 2019), as well as neutral gas clouds with sizes smaller than the broad-line region (Finley et al. 2013; Fathivavsari et al. 2017), has cast doubt on the conclusion that most PDLAs cannot be related to the quasar itself. Here, we show that such neutral gas not only exists but can be naturally interpreted as part of a cycling process within the framework of chaotic cold accretion (CCA, Gaspari & Sądowski 2017). The ubiquitous presence of strong N v and O vi absorption in all the spectra shown in Figures 6 and 9, together with the detection of Si ii* absorption, further supports this interpretation.

We do not expect the gas in Ghostly systems to be in equilibrium. The large dispersion of the H I absorption lines ($b > 100 \text{ km s}^{-1}$) suggests the gas be part of a flow in which condensations can appear under the action of thermal instabilities (Gaspari & Sądowski 2017) or in the process of the disruption of a molecular cloud by an outflow (Laužikas & Zubovas 2024). A constraint of about 10⁵ yr on the typical active galactic nucleus (AGN) phase lifetime is inferred from the time lag between the moment when the AGN central engine switches on and becomes visible in X-rays, and the time required for the AGN to photo-ionise a large fraction of its host galaxy (Schawinski et al. 2015). This is of the same order of magnitude as the expected photo-evaporation time of a Ghostly system and in line with the CCA scenario.

In summary, the kinematical structures we have unveiled suggest a scenario in which AGN-driven outflows interact with a turbulent, multiphase ISM rather than a smooth medium. The hot, energy-driven wind percolates through low-density channels while simultaneously compressing denser clouds. Some of these cold, overdense clumps are accelerated and become part of the outflow, while others survive but are not sufficiently accelerated and eventually fall back towards the nucleus, forming a “fountain” flow. The outflow also injects turbulence, driving shocks and shear that can both destroy some clouds and generate new cold overdensities through radiative cooling. As a result, AGN feedback in such a medium is highly anisotropic and cyclical, with simultaneous gas inflow and outflow, rather than a simple, spherical clearing of the ISM.

To gain a deeper understanding of the origin of the gas we observe as Ghostly DLAs, high-resolution spectral data should be obtained to constrain its physical conditions, in particular its chemical composition and dust content but also internal kinematic structure, density and temperature.

Acknowledgements. This work was supported in part by the Agence Nationale de la Recherche (ANR, France) under contract ANR-22-CE31-0009. We thank Camille Noûs (Laboratoire Cogitamus) for inappreciable and often unnoticed discussions, advice and support. Funding for the Sloan Digital Sky Survey IV has been provided by the Alfred P. Sloan Foundation, the U.S. Department of Energy Office of Science, and the Participating Institutions.

References

Ahumada, R., Allende Prieto, C., Almeida, A., et al. 2020, *ApJS*, 249, 3
 Arav, N., Liu, G., Xu, X., et al. 2018, *ApJ*, 857, 60
 Arav, N., Xu, X., Miller, T., Kriss, G. A., & Plesha, R. 2020, *ApJS*, 247, 37
 Aromal, P., Srianand, R., & Petitjean, P. 2024, *MNRAS*, 527, 12298
 Balashev, S. A., Ledoux, C., Noterdaeme, P., et al. 2023, *MNRAS*, 524, 5016
 Balashev, S. A., Ledoux, C., Noterdaeme, P., et al. 2020, *MNRAS*, 497, 1946
 Belli, S., Park, M., Davies, R. L., et al. 2024, *Nature*, 630, 54
 Bluck, A. F. L., Piotrowska, J. M., & Maiolino, R. 2023, *ApJ*, 944, 108
 Borguet, B. C. J., Arav, N., Edmonds, D., Chamberlain, C., & Benn, C. 2013, *ApJ*, 762, 49
 Bu, D.-F. & Yang, X.-H. 2021, *ApJ*, 921, 100
 Cattaneo, A., Faber, S. M., Binney, J., et al. 2009, *Nature*, 460, 213
 Chabanier, S., Etourneau, T., Le Goff, J.-M., et al. 2022, *ApJS*, 258, 18

Crenshaw, D. M., Kraemer, S. B., & George, I. M. 2003, *ARA&A*, 41, 117
 Dai, X., Bhatiani, S., & Chen, B. 2020, *MNRAS*, 495, 460
 Davies, R. L., Belli, S., Park, M., et al. 2024, *MNRAS*, 528, 4976
 Dawson, K. S., Kneib, J.-P., Percival, W. J., et al. 2016, *AJ*, 151, 44
 Dubois, Y., Gavazzi, R., Peirani, S., & Silk, J. 2013, *MNRAS*, 433, 3297
 Dubois, Y., Peirani, S., Pichon, C., et al. 2016, *MNRAS*, 463, 3948
 Ellison, S. L., Prochaska, J. X., Hennawi, J., et al. 2010, *MNRAS*, 406, 1435
 Ellison, S. L., Prochaska, J. X., & Mendel, J. T. 2011, *MNRAS*, 412, 448
 Ellison, S. L., Yan, L., Hook, I. M., et al. 2002, *A&A*, 383, 91
 Fabian, A. C., Vasudevan, R. V., Mushotzky, R. F., Winter, L. M., & Reynolds, C. S. 2009, *MNRAS*, 394, L89
 Fathivavsari, H. 2020, *ApJ*, 901, 123
 Fathivavsari, H., Petitjean, P., Zou, S., et al. 2017, *MNRAS*, 466, L58
 Faucher-Giguère, C.-A. & Quataert, E. 2012, *MNRAS*, 425, 605
 Filiz Ak, N., Brandt, W. N., Hall, P. B., et al. 2012, *ApJ*, 757, 114
 Finley, H., Petitjean, P., Pâris, I., et al. 2013, *A&A*, 558, A111
 Förster Schreiber, N. M., Übler, H., Davies, R. L., et al. 2019, *ApJ*, 875, 21
 Gaspari, M., McDonald, M., Hamer, S. L., et al. 2018, *ApJ*, 854, 167
 Gaspari, M. & Sądowski, A. 2017, *ApJ*, 837, 149
 Gibson, R. R., Jiang, L., Brandt, W. N., et al. 2009, *ApJ*, 692, 758
 Gofford, J., Reeves, J. N., McLaughlin, D. E., et al. 2015, *MNRAS*, 451, 4169
 Guimaraes, R., Petitjean, P., Rollinde, E., et al. 2007, *MNRAS*, 377, 657
 Gupta, N., Srianand, R., Momjian, E., et al. 2022, *ApJ*, 927, L24
 Han, S., Krogager, J.-K., Ledoux, C., et al. 2026, *A&A*, 705, A123
 Hennawi, J. F. & Prochaska, J. X. 2007, *ApJ*, 655, 735
 Hennawi, J. F., Prochaska, J. X., Kollmeier, J., & Zheng, Z. 2009, *ApJ*, 693, L49
 Jiang, P., Zhou, H., Pan, X., et al. 2016, *ApJ*, 821, 1
 Laha, S., Guainazzi, M., Dewangan, G. C., Chakravorty, S., & Kembhavi, A. K. 2014, *MNRAS*, 441, 2613
 Laha, S., Reynolds, C. S., Reeves, J., et al. 2021, *Nature Astronomy*, 5, 13
 Laloux, B. & Petitjean, P. 2021, *MNRAS*, 502, 3855
 Laor, A. & Brandt, W. N. 2002, *ApJ*, 569, 641
 Laužikas, M. & Zubovas, K. 2024, *A&A*, 690, A396
 Leung, G. C. K., Coil, A. L., Aird, J., et al. 2019, *ApJ*, 886, 11
 Lyke, B. W., Higley, A. N., McLane, J. N., et al. 2020, *ApJS*, 250, 8
 Marconcini, C., Marconi, A., Cresci, G., et al. 2025, *Nature Astronomy*, 9, 907
 Morganti, R., Oosterloo, T., Schulz, R., Tadhunter, C., & Raymond Oonk, J. B. 2020, in *IAU Symposium*, Vol. 342, *Perseus in Sicily: From Black Hole to Cluster Outskirts*, ed. K. Asada, E. de Gouveia Dal Pino, M. Giroletti, H. Nagai, & R. Nemmen, 85–89
 Murray, N. & Chiang, J. 1995, *ApJ*, 454, L105
 Noterdaeme, P., Balashev, S., Cuellar, R., et al. 2023, *A&A*, 673, A89
 Noterdaeme, P., Balashev, S., Krogager, J.-K., et al. 2019, *A&A*, 627, A32
 Noterdaeme, P., Petitjean, P., Carithers, W. C., et al. 2012, *A&A*, 547, L1
 Pan, X., Zhang, S., Zhou, H., et al. 2018, *ApJ*, 863, 198
 Pâris, I., Petitjean, P., Aubourg, É., et al. 2018, *A&A*, 613, A51
 Perrotta, S., D’Odorico, V., Prochaska, J. X., et al. 2016, *MNRAS*, 462, 3285
 Piotrowska, J. M., Bluck, A. F. L., Maiolino, R., & Peng, Y. 2022, *MNRAS*, 512, 1052
 Prochaska, J. X. 2006, *ApJ*, 650, 272
 Prochaska, J. X., Chen, H.-W., & Bloom, J. S. 2006, *ApJ*, 648, 95
 Prochaska, J. X. & Hennawi, J. F. 2009, *ApJ*, 690, 1558
 Prochaska, J. X., Hennawi, J. F., & Herbert-Fort, S. 2008, *ApJ*, 675, 1002
 Rix, S. A., Pettini, M., Steidel, C. C., et al. 2007, *ApJ*, 670, 15
 Rojas-Ruiz, S., Momjian, E., Davies, F. B., et al. 2025, *ApJ*, 985, 34
 Rupke, D. S. N., Thomas, A. D., & Dopita, M. A. 2021, *MNRAS*, 503, 4748
 Schawinski, K., Koss, M., Berney, S., & Sartori, L. F. 2015, *MNRAS*, 451, 2517
 Schaye, J., Crain, R. A., Bower, R. G., et al. 2015, *MNRAS*, 446, 521
 Silva, A. I. & Viegas, S. M. 2002, *MNRAS*, 329, 135
 Springel, V., Di Matteo, T., & Hernquist, L. 2005, *MNRAS*, 361, 776
 Srianand, R. & Petitjean, P. 2000, *A&A*, 357, 414
 Temple, M. J., Rankine, A. L., Banerji, M., et al. 2024, *MNRAS*, 532, 424
 Tombesi, F., Cappi, M., Reeves, J. N., et al. 2013, *MNRAS*, 430, 1102
 Tombesi, F., Cappi, M., Reeves, J. N., et al. 2011, *ApJ*, 742, 44
 Vivek, M. & Wylezalek, D. 2025, *A&A*, 695, L22
 Vreeswijk, P. M., Ledoux, C., Smette, A., et al. 2007, *A&A*, 468, 83
 Wampler, E. J., Chugai, N. N., & Petitjean, P. 1995, *ApJ*, 443, 586
 Weymann, R. J., Carswell, R. F., & Smith, M. G. 1981, *ARA&A*, 19, 41
 Wolfe, A. M., Prochaska, J. X., & Gawiser, E. 2003, *ApJ*, 593, 215
 Wu, Q. & Shen, Y. 2022, *ApJS*, 263, 42
 Wu, S., Shi, X., Kalita, N., et al. 2024, *MNRAS*, 532, 4703
 Xie, X., Zhou, H., Pan, X., et al. 2018, *ApJ*, 858, 32
 Zakamska, N. L., Hamann, F., Pâris, I., et al. 2016, *MNRAS*, 459, 3144